Available online at www.sciencedirect.com
ScienceDirect
Journal of Power Sources 171 (2007) 585–600
JOURNAL OF POWER SOURCES
www.elsevier.com/locate/jpowsour

Two-dimensional dynamic simulation of a direct internal reforming solid oxide fuel cell

Jun Li *, Guang-Yi Cao, Xin-Jian Zhu, Heng-Yong Tu

Institute of Fuel Cell, Department of Automation, Shanghai Jiao Tong University, Shanghai 200030, PR China

Received 17 May 2007; received in revised form 10 July 2007; accepted 10 July 2007
Available online 19 July 2007

Abstract

This study presents a two-dimensional mathematical model of a direct internal reforming solid oxide fuel cell (DIR-SOFC) stack which is based on the reforming reaction kinetics, electrochemical model and principles of mass and heat transfer. To stimulate the model and investigate the steady and dynamic performances of the DIR-SOFC stack, we employ a computational approach and several cases are used including standard conditions, and step changes in fuel flow rate, air flow rate and stack voltage. The temperature distribution, current density distribution, gas species molar fraction distributions and dynamic simulation for a cross-flow DIR-SOFC are presented and discussed. The results show that the dynamic responses are different at each point in the stack. The temperature gradients as well as the current density gradients are large in the stack, which should be considered when designing a stack. Further, a moderate increase in the fuel flow rate improves the performances of the stack. A decrease in the air flow rate can raise the stack temperature and increase fuel and oxygen utilizations. An increased output voltage reduces the current density and gas utilizations, resulting in a decrease in the temperature.

Keywords: Direct internal reforming solid oxide fuel cell; Dynamic simulation; Model

1. Introduction

The solid oxide fuel cell (SOFC) functions at high temperature via a completely solid-state ion-conducting electrolyte [1,2]. With the capability of internal reforming, the SOFC can be directly fueled with pure hydrogen, natural gas, coal gas and other hydrocarbons [1–3]. Further, the exhaust gas generated by the SOFC contains a lot of heat, steam and unused fuel, which can be conveniently recycled in the power plant when the SOFC is in use with gas turbines. Therefore, with such high energy generating efficiency and low pollution, the SOFC has been considered to be one of the most promising fuel cells for future power plants [1,2].

Several models have been proposed to simulate and analyze the operating conditions of SOFC stacks [4–15]. Costamagna and Honegger [8] presented and validated a simulation model for a SOFC stack integrated with an air pre-heater. Padulles et al. [9] demonstrated two other SOFC stack models to simulate the power system and the power conditioning units of the plant, respectively. However, dynamic responses of the temperature and current density in these simulated models are not clear. Recently, a novel one-dimensional dynamic model of a tubular SOFC with external and internal reforming was proposed by Jiang et al. [10]. Using this dynamic model, SOFC characteristics such as the cell voltage, temperature and power under different conditions can be predicted. However, the distribution of parameters such as current density and gas concentration across the cell is not known.

Compared with indirect internal reforming SOFC (IIR-SOFC) and hydrogen-fueled SOFC stacks, a direct internal reforming solid oxide fuel cell (DIR-SOFC) stack has unique reaction kinetics, in which the reforming reactions interact with concurrent electrochemical reactions [14–18]. It is well known that the dynamic performances and the parameter distribution of the stack are crucial for designing and controlling DIR-SOFC. In this regard, a one-dimensional DIR-SOFC stack model (anode-supported with intermediate temperature) has been used for simulation of DIR-SOFC [14,15]. Further, using this model, the one-dimensional steady-state parameter distribution and dynamic response to several current density step-changes can

* Corresponding author. Tel.: +86 21 62932154.
E-mail addresses: lijun05@sjtu.edu.cn, jun.li.fc@gmail.com (J. Li).

0378-7753/$ – see front matter © 2007 Elsevier B.V. All rights reserved.
doi:10.1016/j.jpowsour.2007.07.029

Nomenclature

A	stoichiometric matrix
A_{k_n}	pre-exponential factor for rate coefficient k_n
$A_{K_j^{ad}}$	pre-exponential factor for K_j^{ad}
B	coefficient matrix
C_p	specific heat capacity ($kJ\,kg^{-1}\,K^{-1}$ for solid, $kJ\,mol^{-1}\,K^{-1}$ for gas)
$\vec{C}_p$	specific heat capacity vector
E	Nernst voltage (V)
E_n	activation energy of reaction n ($kJ\,mol^{-1}$)
F_{Far}	Faraday constant ($96{,}485\,C\,mol^{-1}$)
$\vec{F}$	gas flow rate vector
$\Delta\bar{g}_f^0$	change of Gibbs free energy ($kJ\,mol^{-1}$)
h	gas enthalpy ($kJ\,mol^{-1}$)
ΔH_j^{ad}	enthalpy change of adsorption ($kJ\,mol^{-1}$)
i	current density ($A\,m^{-2}$)
i_0	exchange current density ($A\,m^{-2}$)
i_L	limiting current density ($A\,m^{-2}$)
j	gas component
k_n	rate coefficient for reforming reaction n
K	equilibrium constant
K_j^{ad}	adsorption constants for gas component j
m	number of moles of electrons transferred per mole of reactant
n	reaction
P	partial pressure (bar)
q	heat generation or transfers ($kJ\,m^{-2}\,s^{-1}$)
r	reaction rate ($mol\,s^{-1}\,m^{-2}$)
$\vec{r}$	reaction rate vector
R	gas constant ($8.314\,J\,K^{-1}\,mol^{-1}$)
S_h	volumetric rate of heat generation ($kJ\,m^{-3}\,s^{-1}$)
T	temperature (K)
$\vec{T}$	temperature vector
V	output voltage (V)
$\vec{V}$	gas velocity vector

Greek symbols

α^{an}, α^{ca}	charge transfer coefficients
β_1, β_2	coefficients for η^{ohm}
γ^{an}, γ^{ca}	coefficients for i_0^{an} and i_0^{ca}
δ	material thickness (m)
$\vec{\delta}$	thickness vector
ε	emissivity
ζ	thermal conductivity ($W\,m^{-1}\,K^{-1}$)
η^{ohm}	ohmic polarization (V)
η^{act}	activation polarization (V)
η^{conc}	concentration loss (V)
ξ	convective heat transfer coefficient ($W\,m^{-2}\,K^{-1}$)
ρ	density ($kg\,m^{-3}$ for solid, $mol\,m^{-3}$ for gas)
$\vec{\rho}$	density vector
σ_B	Stefan–Boltzmann constant ($5.676 \times 10^{-8}\,W\,m^{-2}\,K^{-4}$)

Superscripts

an	anode
ca	cathode
in	inlet
lp	lower bipolar plate
out	outlet
pa	upper bipolar plate surface
pc	lower bipolar plate surface
re	reforming
s	SOLID (anode-electrolyte-cathode)
sa	anodic surface of SOLID
sc	cathodic surface of SOLID
up	upper bipolar plate

Subscripts

I	reaction I
II	reaction II
III	reaction III
conv	convection
e	electrochemical reaction
rad	radiation

be generated. However, because the two-dimensional situation is not considered, the one-dimensional model is only applicable to co- and counter-flow operation but not to cross-flow operation.

In this study, we have constructed a two-dimensional dynamic model of the DIR-SOFC. This dynamic model is generated based on the methane steam-reforming kinetics, mechanism of chemical-to-electrical conversion, energy balance and mass conservation. To describe the dynamic behavior in the cross-flow stack of this model, we have utilized multiple partial differential equations (PDEs). We have also employed an alternative computational method to find the numerical solutions for the PDEs. Further, several cases are presented to study the steady and dynamic performances of the DIR-SOFC using this two-dimensional dynamic model.

The present study is organized into five sections. In Section 2, the mathematical model is established following a brief description of the DIR-SOFC. In Section 3, a numerical method is used to solve the PDEs obtained in Section 2. In Section 4, the steady-state distributions (the temperature, current density and gas species molar fractions), as well as the dynamic responses of the stack for four cases, are presented and discussed. Section 5 concludes the paper and gives a perspective on the future research.

2. Modeling of a DIR-SOFC

The working principles of a DIR-SOFC stack are illustrated in Fig. 1. The electrolyte, which divides the stack into two electrodes, acts as an electronic barrier and avoids the direct chemical reaction of the fuel at the anode with the oxygen at the cathode. At the cathode, molecular oxygen combines with electrons and is reduced to negatively charged ions (O^{2-}) with the aid of a catalyst [1,2].

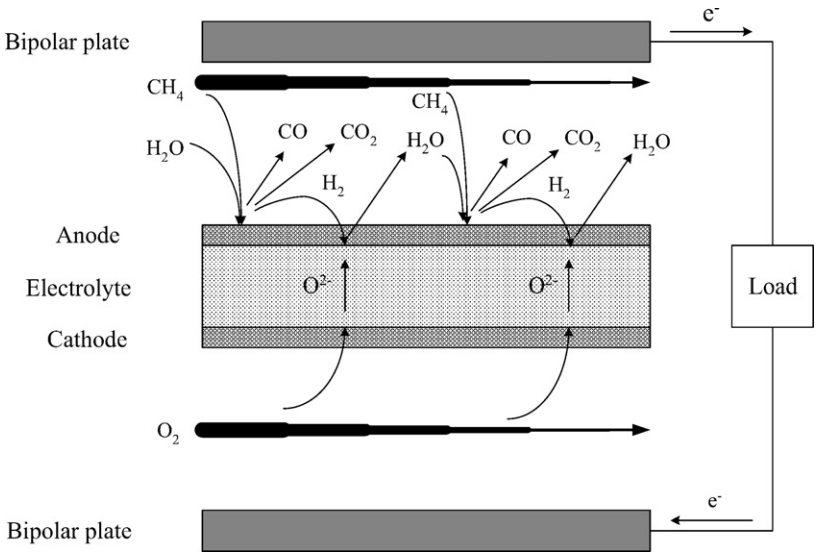

Fig. 1. Diagram of a DIR-SOFC stack.

Cathodic electrochemical reaction:

$$\frac{1}{2}O_2 + 2e^- \rightarrow O^{2-} \quad (1)$$

The steam–methane gas mixture flows in the anode of the DIR-SOFC and be reformed inside to provide the hydrogen and carbon monoxide for the electrochemical reaction to generate electricity [1,2]. The reactions at the anode of the DIR-SOFC are more complex than that using the pure hydrogen fuel due to coupling between reforming reactions and electrochemical reactions.

At the anode, hydrogen and carbon monoxide react with oxygen ions to form water and carbon dioxide, respectively, and release electrons.

Anodic electrochemical reaction:

$$H_2 + O^{2-} \rightarrow H_2O + 2e^- \quad (2)$$

$$CO + O^{2-} \rightarrow CO_2 + 2e^- \quad (3)$$

Electrons released at the anode pass through the bipolar plate to the cathode of the next cell in the series, or follow the external circuit to drive the load, before finally returning to the cathode.

Bipolar plates, with machined flow channels, clamp together the anode–electrolyte–cathode construction and provide the main structural support of the fuel cell. They also collect the current generated by the electrochemical reaction.

Some assumptions are necessary in the derivation of the two-dimensional DIR-SOFC model.

(1) All gases are assumed to be ideal gases.
(2) The anode, electrolyte and cathode layers, which are clamped together, are assumed to be horizontally homogeneous. The anode–electrolyte–cathode is denoted by the abbreviation SOLID.
(3) The walls of gas channels are smooth.
(4) Constant pressure is maintained within the gas channels.
(5) Methane does not directly participate in the electrochemical reaction at the anode.
(6) The stack works in the cross-flow mode.

2.1. Reforming model

The principal reactions in the methane steam-reforming are listed as follows [16–18]:

$$\text{Reaction I: } CH_4 + 2H_2O \leftrightarrow CO_2 + 4H_2 \quad (4)$$
$$\text{Reaction II: } CH_4 + H_2O \leftrightarrow CO + 3H_2 \quad (5)$$
$$\text{Reaction III: } CO + H_2O \leftrightarrow CO_2 + H_2 \quad (6)$$

In the reforming process, reactions I and II are the dominant reactions with products mainly comprising H_2, CO and CO_2. Both reactions are endothermic. Reaction III is the water-gas shift reaction. The electrochemical reaction is exothermic and supplies heat and steam to the endothermic reactions. Below 900 K, Reaction I dominates and the methane is mostly converted to carbon dioxide. Above 900 K, reaction II becomes predominant. The reversible reactions obey the laws of chemical equilibrium. The equilibrium constants for reactions I–III can be computed by three functions of temperature [11] which are given by

$$K_I = \frac{P_{CO_2} P_{H_2}^4}{P_{CH_4} P_{H_2O}^2} = \exp\left(-\frac{22,430}{T} + 26.078\right), \quad (7)$$

$$K_{II} = \frac{P_{CO} P_{H_2}^3}{P_{CH_4} P_{H_2O}} = \exp\left(-\frac{26,830}{T} + 30.114\right), \quad (8)$$

$$K_{III} = \frac{P_{CO_2} P_{H_2}}{P_{CO} P_{H_2O}} = \exp\left(\frac{4400}{T} - 4.036\right), \quad (9)$$

where P_{CH_4}, P_{H_2}, P_{CO}, P_{CO_2} and P_{H_2O} are the partial pressures of CH_4, H_2, CO, CO_2 and H_2O, respectively, when the chemical reactions reach equilibriums. T is the temperature. As can be seen from Eqs. (7)–(9), the consumption of the hydrogen

caused by the electrochemical reaction can shift the reforming reaction in the forward direction. The methane steam-reforming is preferably carried out under the conditions of high temperature and high steam-to-carbon ratio (S/C). Nickel in the SOFC stack is used as the internal reforming catalyst to accelerate the reforming reactions.

The reforming reaction rates are computed by following equations proposed in [16].

$$r_{\mathrm{I}}^{\mathrm{re}} = \frac{k_{\mathrm{I}}}{P_{\mathrm{H_2}}^{\mathrm{an}\,3.5}(\mathrm{DEN})^2}\left(P_{\mathrm{CH_4}}^{\mathrm{an}} P_{\mathrm{H_2O}}^{\mathrm{an}^2} - \frac{P_{\mathrm{H_2}}^{\mathrm{an}\,4} P_{\mathrm{CO_2}}^{\mathrm{an}}}{K_{\mathrm{I}}}\right), \tag{10}$$

$$r_{\mathrm{II}}^{\mathrm{re}} = \frac{k_{\mathrm{II}}}{P_{\mathrm{H_2}}^{\mathrm{an}^{2.5}}(\mathrm{DEN})^2}\left(P_{\mathrm{CH_4}}^{\mathrm{an}} P_{\mathrm{H_2O}}^{\mathrm{an}} - \frac{P_{\mathrm{H_2}}^{\mathrm{an}^3} P_{\mathrm{CO}}^{\mathrm{an}}}{K_{\mathrm{II}}}\right), \tag{11}$$

$$r_{\mathrm{III}}^{\mathrm{re}} = \frac{k_{\mathrm{III}}}{P_{\mathrm{H_2}}^{\mathrm{an}}(\mathrm{DEN})^2}\left(P_{\mathrm{CO}}^{\mathrm{an}} P_{\mathrm{H_2O}}^{\mathrm{an}} - \frac{P_{\mathrm{H_2}}^{\mathrm{an}} P_{\mathrm{CO_2}}^{\mathrm{an}}}{K_{\mathrm{III}}}\right). \tag{12}$$

The superscript "an" denotes the anode. k_n, with $n = \mathrm{I,II,III}$, are the rate coefficients for the reforming reactions and are calculated by

$$k_n = A_{k_n} \exp\left(-\frac{E_n}{RT}\right), \quad n = \mathrm{I,II,III}, \tag{13}$$

where A_{k_n} is the pre-exponential factor of the rate coefficient k_n, E_n is the activation energy of the reaction, and R is the gas constant ($8.314\,\mathrm{J\,K^{-1}\,mol^{-1}}$). DEN is defined as

$$\mathrm{DEN} = 1 + K_{\mathrm{CO}}^{\mathrm{ad}} P_{\mathrm{CO}}^{\mathrm{an}} + K_{\mathrm{H_2}}^{\mathrm{ad}} P_{\mathrm{H_2}}^{\mathrm{an}} + K_{\mathrm{CH_4}}^{\mathrm{ad}} P_{\mathrm{CH_4}}^{\mathrm{an}} + K_{\mathrm{H_2O}}^{\mathrm{ad}} \frac{P_{\mathrm{H_2O}}^{\mathrm{an}}}{P_{\mathrm{H_2}}^{\mathrm{an}}} \tag{14}$$

In Eq. (14), $K_{\mathrm{CO}}^{\mathrm{ad}}$, $K_{\mathrm{H_2}}^{\mathrm{ad}}$, $K_{\mathrm{CH_4}}^{\mathrm{ad}}$ and $K_{\mathrm{H_2O}}^{\mathrm{ad}}$, the adsorption constants for CO, H_2, $CH_4$and H_2O, respectively, are computed by

$$K_j^{\mathrm{ad}} = A_{K_j^{\mathrm{ad}}} \exp\left(-\frac{\Delta H_j^{\mathrm{ad}}}{RT}\right), \quad j = \mathrm{CO,H_2,CH_4,H_2O}, \tag{15}$$

where $A_{K_j^{\mathrm{ad}}}$ is the pre-exponential factor of the adsorption constant K_j^{ad}, and ΔH_j^{ad} is the enthalpy change of adsorption.

2.2. Chemical-to-electrical conversion of SOFC

The electrochemical oxidation of CO is not considered in our study, because data in the literature show that the electrochemical oxidation of hydrogen is faster than that of CO [18]. Hence, the Nernst voltage E is mainly dependent on the electrochemical reaction of H_2:

$$E = \frac{-\Delta \bar{g}_f^0}{2F_{\mathrm{Far}}} + \frac{RT}{2F_{\mathrm{Far}}} \ln\left(\frac{P_{\mathrm{H_2}}^{\mathrm{an}} P_{\mathrm{O_2}}^{\mathrm{ca}\,1/2}}{P_{\mathrm{H_2O}}^{\mathrm{an}}}\right), \tag{16}$$

where $\Delta \bar{g}_f^0$ is the change in molar Gibbs free energy of formation at standard pressure, and F_{Far} is the Faraday constant ($96{,}485\,\mathrm{C\,mol^{-1}}$)[1]. The superscript "ca" denotes the cathode. The pressure unit is bar.

The cell output voltage, reduced by the ohmic polarization η^{ohm}, the activation polarization η^{act} and the concentration loss η^{conc}, can be written as

$$V = E - \eta^{\mathrm{ohm}} - \eta^{\mathrm{act}} - \eta^{\mathrm{conc}}. \tag{17}$$

The ohmic polarization can be expressed as

$$\eta^{\mathrm{ohm}} = i \cdot \Omega, \tag{18}$$

$$\Omega = \delta \cdot \beta_1^{-1} \exp\left(\frac{\beta_2}{T}\right), \tag{19}$$

where δ is the material thickness, and i is the current density. The coefficients β_1 and β_2 can be obtained by curve fitting the simulated data proposed in Ref. [8]. The ohmic polarization depends on the physical configuration of the SOFC and on the operating temperature.

The electrode activation polarizations can be described by the Butler–Volmer equation [8]:

$$i = i_0\left[\exp\left(\alpha^{\mathrm{an}}\frac{F_{\mathrm{Far}}}{RT^{\mathrm{s}}}\eta^{\mathrm{act}}\right) - \exp\left(\alpha^{\mathrm{ca}}\frac{F_{\mathrm{Far}}}{RT^{\mathrm{s}}}\eta^{\mathrm{act}}\right)\right], \tag{20}$$

where α^{an} and α^{ca} are the charge transfer coefficients of the anode and cathode, respectively. The superscript "s"denotes the SOLID. The exchange current density i_0, which reflects the electrochemical reaction rate at the equilibrium potential, should be considered at both anode and cathode.

Eqs. (21) and (22), proposed by Yamamura and Mogensen et al. [8,12,13,19,20], are used to calculate the exchange current densities at the anode and cathode, respectively:

$$i_0^{\mathrm{an}} = \gamma^{\mathrm{an}}\left(\frac{P_{\mathrm{H_2}}^{\mathrm{an}}}{P_{\mathrm{ref}}}\right)\left(\frac{P_{\mathrm{H_2O}}^{\mathrm{an}}}{P_{\mathrm{ref}}}\right)\exp\left(-\frac{E_{\mathrm{act}}^{\mathrm{an}}}{RT^{\mathrm{s}}}\right), \tag{21}$$

$$i_0^{\mathrm{ca}} = \gamma^{\mathrm{ca}}\left(\frac{P_{\mathrm{O_2}}^{\mathrm{ca}}}{P_{\mathrm{ref}}}\right)^{0.25}\exp\left(-\frac{E_{\mathrm{act}}^{\mathrm{ca}}}{RT^{\mathrm{s}}}\right), \tag{22}$$

where γ^{an} and γ^{ca} are coefficients, $E_{\mathrm{act}}^{\mathrm{an}}$ and $E_{\mathrm{act}}^{\mathrm{ca}}$ are the activation energies. P_{ref} is the reference pressure which is always set as 1 bar.

As can be seen from Eqs. (21) and (22), the temperature and pressure influence the exchange current density. The electrochemical reaction can be accelerated by increasing the operating temperature and the partial pressures.

A formula related to the temperature and the current density is used to estimate the concentration loss according to the Nernst equation [2]:

$$\eta^{\mathrm{conc}} = -\frac{RT}{mF_{\mathrm{Far}}}\ln\left(1 - \frac{i}{i_{\mathrm{L}}}\right), \tag{23}$$

where i_{L} is the limiting current density.

The consumption rates of H_2 and O_2 due to the electrochemical reaction ($r_{\mathrm{H_2}}^{\mathrm{an}}$, $r_{\mathrm{O_2}}^{\mathrm{ca}}$) are determined by the current density. The consumption rate of H_2 is twice that of O_2. A larger current density results in faster consumption rates of H_2 and O_2 in the electrochemical reaction.

$$r_{\mathrm{H_2}}^{\mathrm{an}} = \frac{i}{2F_{\mathrm{Far}}}, \tag{24}$$

$$r_{O_2}^{ca} = \frac{i}{4F_{Far}}. \quad (25)$$

2.3. Mass conservation

The gas flow rates at the anode and cathode will change with the time and flow distance due to fuel and oxygen consumptions in the reforming and electrochemical reactions.

$$\vec{F}^{in} + A \cdot \vec{r} \cdot B = \vec{F}^{out}. \quad (26)$$

$\vec{F}$ is the gas flow rate vector including the vectors of the anodic and cathodic flow rates.

$$\vec{F} = \begin{bmatrix} \vec{F}^{an} \\ \vec{F}^{ca} \end{bmatrix}, \quad (27)$$

where

$$\vec{F}^{an} = \left(F_{CH_4}, F_{CO}, F_{CO_2}^{an}, F_{H_2O}^{an}, F_{H_2}\right)^T, \quad (28)$$

$$\vec{F}^{ca} = \left(F_{O_2}, F_{N_2}, F_{H_2O}^{ca}, F_{CO_2}^{ca}\right)^T. \quad (29)$$

$\vec{r}$ is the reaction rate vector including the rates of reactions at the anode and cathode.

$$\vec{r} = \begin{bmatrix} \vec{r}^{an} \\ r^{ca} \end{bmatrix}, \quad (30)$$

where

$$\vec{r}^{an} = \left(r_I^{re}, r_{II}^{re}, r_{III}^{re}, r_{H_2}^{an}\right)^T, \quad (31)$$

$$r^{ca} = r_{O_2}^{ca}. \quad (32)$$

A is the stoichiometric matrix.

$$A = \begin{bmatrix} A^{an} & 0 \\ 0 & A^{ca} \end{bmatrix}, \quad (33)$$

where

$$A^{an} = \begin{bmatrix} -1 & -1 & 0 & 0 \\ 0 & 1 & -1 & 0 \\ 1 & 0 & 1 & 0 \\ -2 & -1 & -1 & 1 \\ 4 & 3 & 1 & -1 \end{bmatrix}, \quad (34)$$

$$A^{ca} = \begin{bmatrix} -1 \\ 0 \\ 0 \\ 0 \end{bmatrix}. \quad (35)$$

B is the coefficient matrix in which elements are functions of the reaction area.

2.4. Energy balance

A considerable quantity of electrical energy is produced via electrochemical reactions. This is output through the polar plates and can supply electricity to external appliances: this is the motivation behind the development of fuel cells. As well as the electrical power, some energy is lost heating the stack and the rest flows out of the stack with the exhaust gases.

The energy equation for the air and fuel flows can be expressed as

$$\frac{\partial(\rho h)}{\partial t} + \mathrm{div}\left(\rho h \vec{V} - \frac{\zeta \nabla h}{C_p}\right) = S_h, \quad (36)$$

where ρ is the density, h the gas enthalpy, div denotes the divergence, $\vec{V}$ is the gas velocity vector, ∇ denotes the gradient, ζ is the thermal conductivity, C_p is the specific heat capacity and S_h is the volumetric heat generation source or sink.

The energy equation for the SOLID and bipolar plate can be simplified as follows because of the incompressibility of the solid where there is no fluid motion:

$$\rho C_p \frac{\partial T}{\partial t} - \mathrm{div}(\zeta \nabla T) = S_h. \quad (37)$$

The heat generation and transfers between the components of the stack are shown in Fig. 2.

The local heat generated on the SOLID due to the reforming and electrochemical reactions can be expressed by

$$q^s = -\Delta H_e \cdot r_{H_2}^{an} - \Delta H_I^{re} \cdot r_I^{re} - \Delta H_{II}^{re} \cdot r_{II}^{re} - V \cdot i. \quad (38)$$

where the subscript "e"denotes the electrochemical reaction. The rate distributions of the endothermic and exothermic reactions are not uniform in the stack, so q^s can be positive or negative at different positions in the stack.

The heat change, caused by the water-gas shift reaction occurring in the anodic fuel flow, is

$$q_{shift}^{an} = -\Delta H_{III} \cdot r_{III}^{re}. \quad (39)$$

The convective heat fluxes from the SOLID surface to the anodic and cathodic flows are calculated by

$$q_{conv}^{s,an} = \xi^{sa}(T^s - T^{an}), \quad (40)$$

$$q_{conv}^{s,ca} = \xi^{sc}(T^s - T^{ca}), \quad (41)$$

where ξ is the convective heat transfer coefficient. Superscripts "sa"and "sc"denote the anodic and cathodic surfaces of the SOLID, respectively.

The radiant heat fluxes between the SOLID and bipolar plate surfaces are calculated by

$$q_{rad}^{s,up} = \frac{\sigma_B(T^{s4} - T^{up4})}{1/\varepsilon^{sa} + 1/\varepsilon^{up} - 1}, \quad (42)$$

$$q_{rad}^{s,lp} = \frac{\sigma_B(T^{s4} - T^{lp4})}{1/\varepsilon^{sc} + 1/\varepsilon^{lp} - 1}, \quad (43)$$

where σ_B is the Stefan–Boltzmann constant, and ε is the emissivity. Superscripts "up"and "lp"denote the upper and lower bipolar plates, respectively.

No reactions occur on the bipolar plates. Hence, we consider convective heat transfer, thermal radiation and heat conduction in the plates and neglect heat generation.

The convective heat fluxes from the upper and lower bipolar plate surfaces are given by

$$q_{\text{conv}}^{\text{up,an}} = \xi^{\text{pa}}(T^{\text{up}} - T^{\text{an}}), \quad (44)$$

$$q_{\text{conv}}^{\text{lp,ca}} = \xi^{\text{pc}}(T^{\text{lp}} - T^{\text{ca}}), \quad (45)$$

where superscripts "pa"and "pc" denote the surfaces of the upper and lower bipolar plates, respectively.

As Figs. 1 and 2 show, some heat ($q_{\text{react,n}}^{\text{an}}$, $q_{\text{react,n}}^{\text{ca}}$) is carried in the SOLID by the consumed reactant gases, and some heat ($q_{\text{react,n}}^{\text{s}}$) is carried out of the SOLID by the product gases due to reactions at the interfaces of the SOLID and gas flow. The expressions of these heat fluxes corresponding to the various reactions are detailedly given in Appendix A.

3. Computational method

Problems in fluid dynamics usually require solutions of certain PDEs with given boundary conditions. These equations can only be treated analytically in the case of simple boundaries. However, in the DIR-SOFC stack, the fluid governing equations with complex conditions are coupled and nonlinear. Therefore, it is difficult to acquire the exact mathematical solutions for these equations. Alternatively, a computational method is used to find an approximate numerical solution. First, the continuous physical domain is discretized into a set of cells to generate a computational grid. Second, the PDEs are transformed into finite difference equations. Lastly, the solutions of the difference equations at grid nodes are used to approximate the variables of the PDEs [21].

Operating in the cross-flow mode, the fuel flows in the x direction, while the air flows in the y direction which is perpendicular to the x direction. A regular rectangular grid, with grid spacing Δu in the direction of x and Δw in the direction of y, is generated. A regular grid simplifies the discretization of the PDEs, saves computing time, reduces storage requirements, and improves computational accuracy. Combining the formulas derived in Section 2, the model equations are written in matrix form to facilitate programming and processing in the computer (see Appendix A for details).

4. Simulation and discussion

The two-dimensional dynamic model is developed in Matlab. Four cases are used to obtain the steady-state parameter distributions and the dynamic responses of the cross-flow DIR-SOFC under different conditions. Points with dimensionless (x, y) co-ordinates (0.025, 0.05), (1, 0.05), (0.5, 0.5), (0.025, 1), and (1, 1) are chosen as examples to show the dynamic performances at different positions on the SOLID. In addition, the mean temperature, the mean current density and the fuel and oxygen utilizations are important characteristics which must be determined.

Case 1: Using the equations derived in Section 2 and Appendix A, the iteration is started with the initial values listed in Table 1. During the simulation, conditions in the stack evolve after each iteration until they reach a steady state.

The two-dimensional steady-state temperature distribution on the SOLID is illustrated in Fig. 3, and the corresponding contours are shown in Fig. 4. The two-dimensional current density distribution and the corresponding contours are displayed in Figs. 5 and 6, respectively. The molar fraction distributions of CH_4, CO, CO_2, H_2O, $H_2$and O_2 are shown in Figs. 7–12 , respectively.

The methane steam-reforming rate is rapid near the fuel inlet because of the large methane concentration (Fig. 7) and the function of the catalyst. The electrochemical reaction rate of the hydrogen is slow at the

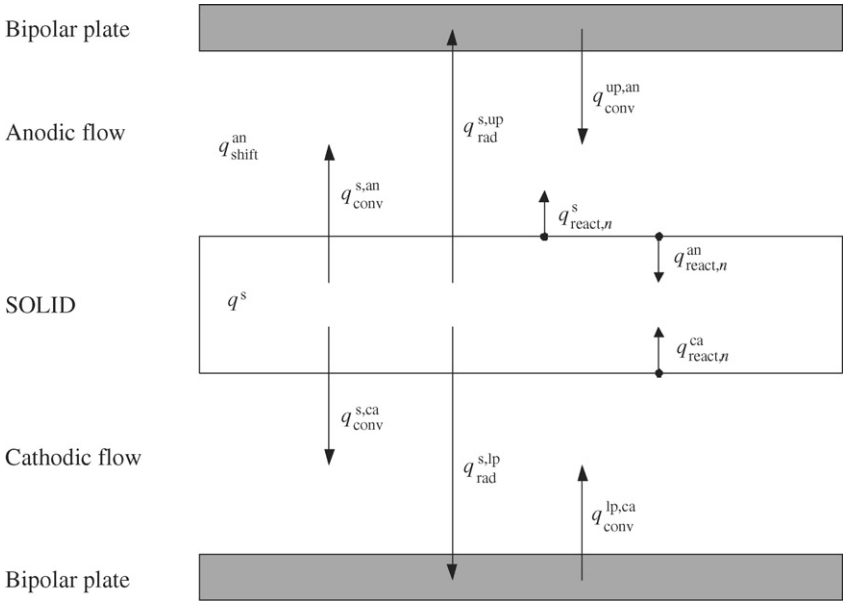

Fig. 2. Diagram of heat generation and transfers in the stack.

Table 1
Initial values of variables and parameters

Item	Value
Fuel flow rate	1.68×10^{-3} mol s^{-1}
Air flow rate	1.43×10^{-2} mol s^{-1}
Inlet fuel temperature	1023 K
Inlet air temperature	1023 K
Upper bipolar plate temperature	1024 K
Lower bipolar plate temperature	1024 K
SOLID temperature	1024 K
Output voltage	0.7 V
Pressure	3 bar
Inlet molar fractions at the anode	
CH_4	28%
CO	1%
CO_2	1%
H_2O	60%
H_2	10%
Inlet molar fractions at the cathode	
O_2	23%
N_2	75%
CO_2	1%
H_2O	1%

inlet due to the low hydrogen concentration (Fig. 11). As a result, the local current density near the fuel inlet is very small (no more than 500 A m^{-2}: Fig. 6). The heat generated in the electrochemical reaction is insufficient to compensate for the thermal losses caused by the endothermic reforming reactions. This results in the temperature drop of the SOLID near the fuel inlet as shown in Figs. 3 and 4. The minimum local temperature is 998 K which is lower than the inlet temperature (1023 K) of the fuel.

The continuous reforming increases the hydrogen concentration along the fuel flow direction (Fig. 11), which results in the acceleration of the electrochemical reaction as well as the rapid increase of the local current density. The reforming rate slows down due to the decrease of methane concentration as shown in Fig. 7. Then, the heat generated by the electrochemical reaction exceeds the reforming thermal losses. Thus, the temperature gradually rises and finally surpasses

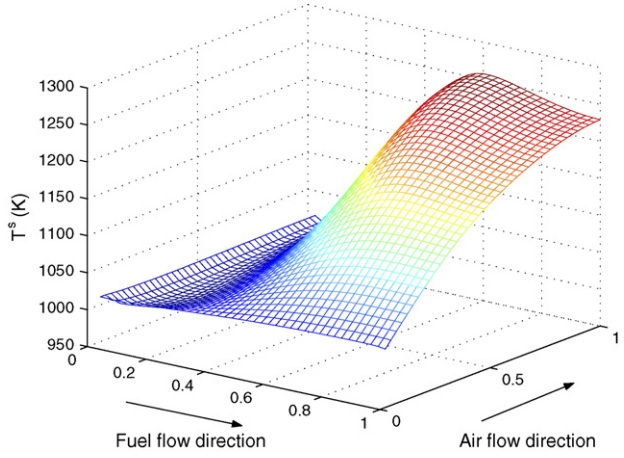

Fig. 3. Two-dimensional temperature distribution in the DIR-SOFC stack.

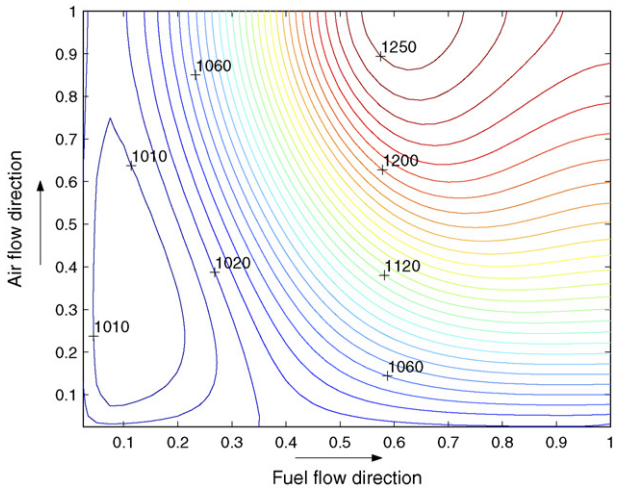

Fig. 4. Temperature (K) contours corresponding to Fig. 3.

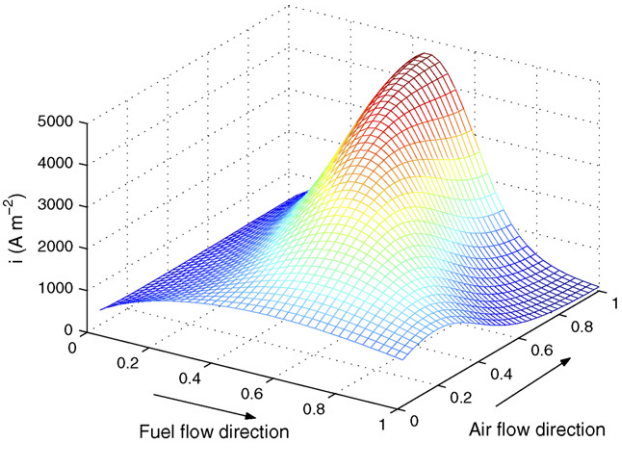

Fig. 5. Two-dimensional current density distribution in the DIR-SOFC stack.

the inlet flow temperature along the fuel flow direction (Figs. 3 and 4). The raised temperature also promotes the electrochemical reaction to increase the current density and to generate more heat.

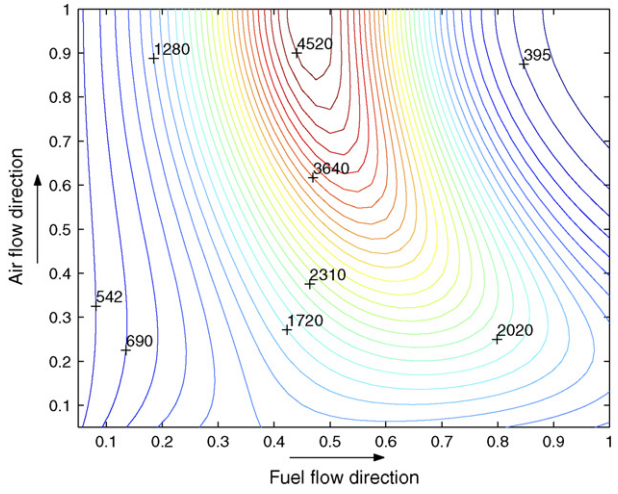

Fig. 6. Current density (A m^{-2}) contours corresponding to Fig. 5.

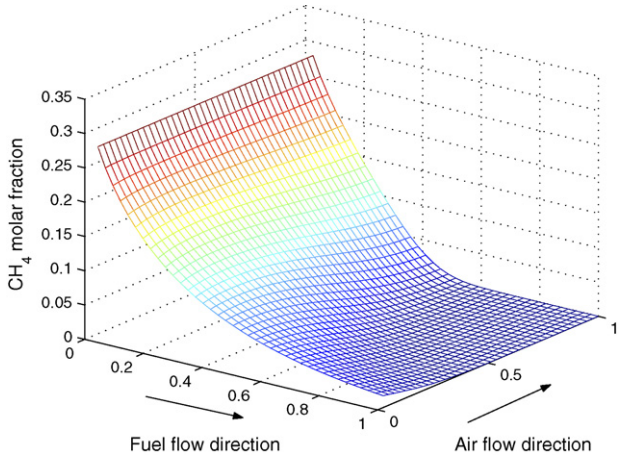

Fig. 7. CH_4 molar fraction distribution.

Most of the methane has been reformed, and the hydrogen concentration begins to decrease, once the fuel reaches the second half of the fuel channel (Figs. 7 and 11, respectively). Therefore, the local current density gradually decreases from the maximum (4668 A m^{-2})along the fuel flow direction near the air outlet (Figs. 5 and 6). The local temperature also declines from the maximum (1257 K) along the same direction, as shown in Figs. 3 and 4.

The temperature rises gradually along the direction of the air flow (Figs. 3 and 4), due to heat loss from

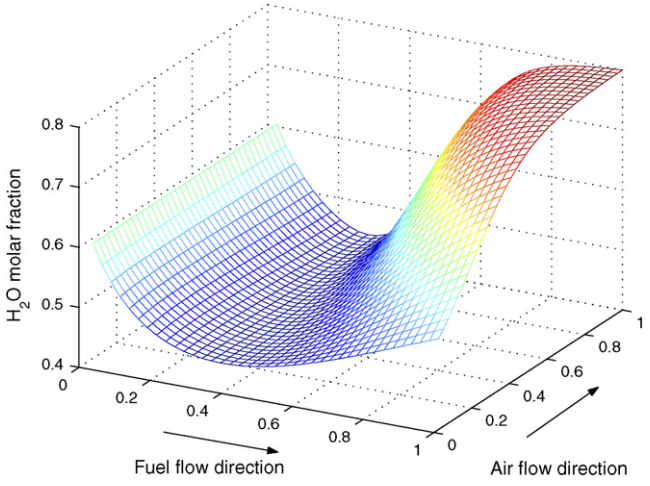

Fig. 10. H_2O molar fraction distribution.

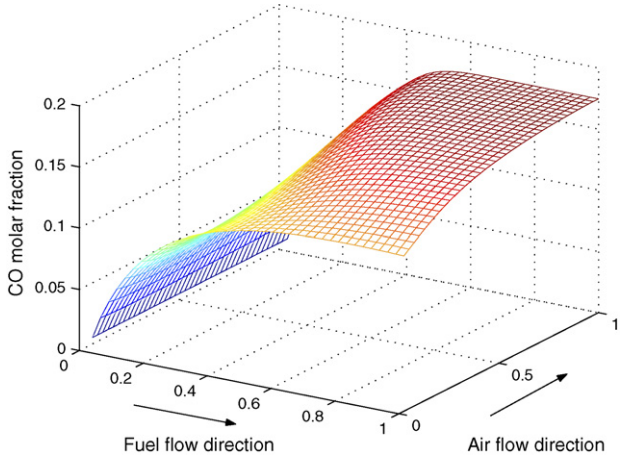

Fig. 8. CO molar fraction distribution.

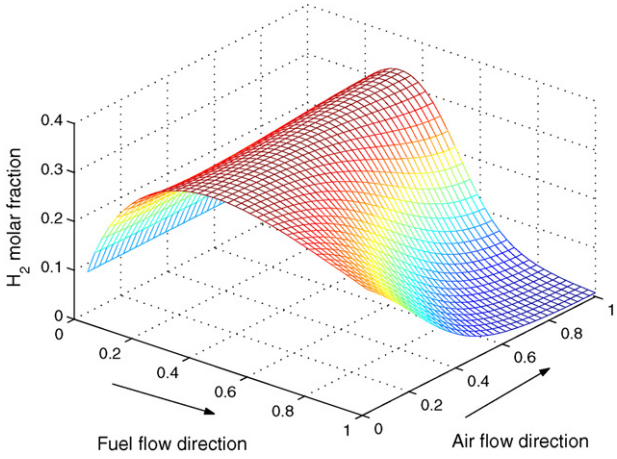

Fig. 11. H_2 molar fraction distribution.

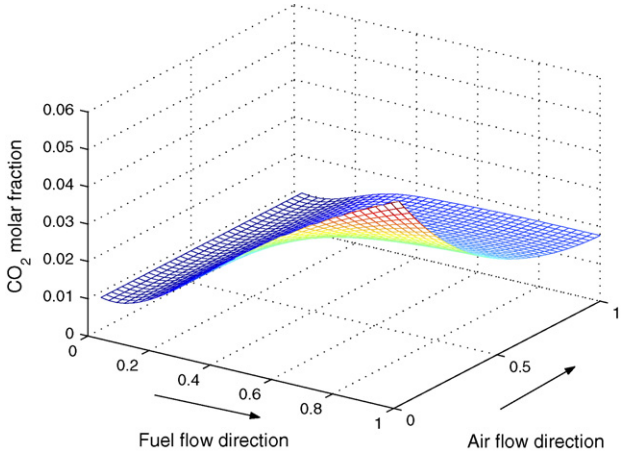

Fig. 9. CO_2 molar fraction distribution.

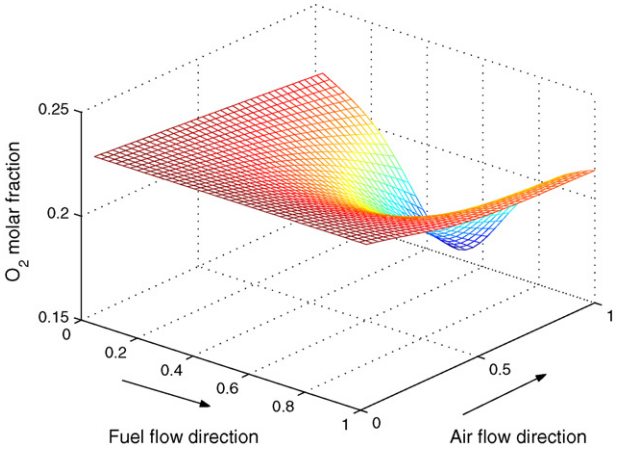

Fig. 12. O_2 molar fraction distribution.

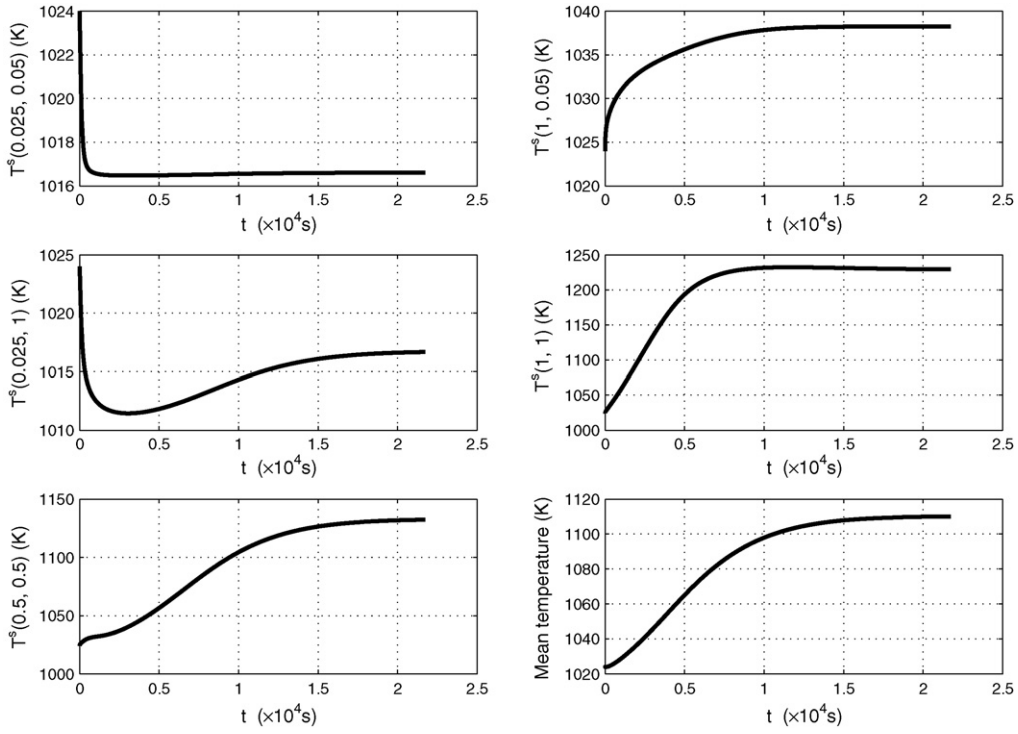

Fig. 13. Dynamic responses of temperature to the initial settings.

the SOLID into the gas flow. This is one of the reasons why the maximum temperature is not at the point of the highest oxygen concentration, but near the air outlet, as shown in Figs. 3 and 12.

The difference between the maximum and minimum temperatures (1257 and 998 K) is 259 K, which indicates a strong temperature gradient in the SOLID. This gradient should be taken as an important factor in the design and control of the stack.

Initial values in the computational algorithm are equivalent to the step changes used to stimulate the model. The iteration process is the response of the

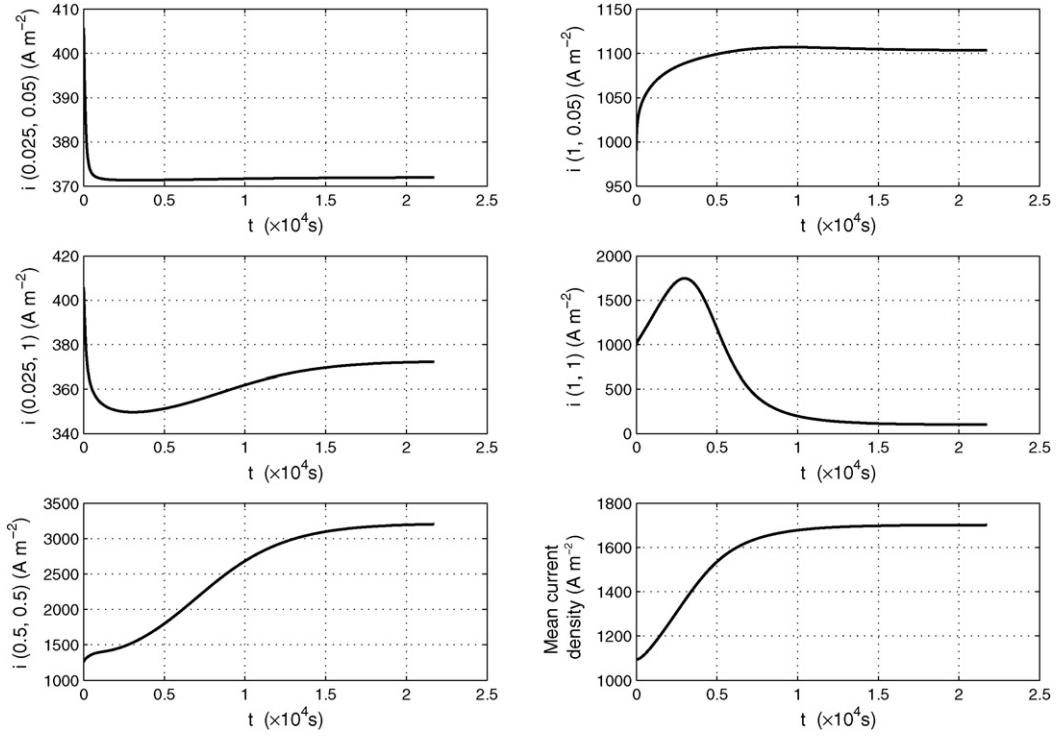

Fig. 14. Dynamic responses of current density to the initial settings.

system to the step change. The dynamic temperature responses at the five representative points to the initial settings are plotted in Fig. 13. The dynamic current density responses are shown in Fig. 14. As can be seen from Fig. 13, it takes about 20,000 s for the mean temperature to reach the stable value (1110 K). However, the time duration from the beginning of the iterations to the steady state at each point is different. Conditions at the point (0.025, 0.05) near the fuel and air inlet approach the stable value rapidly, while other points take more time to stabilize. The plots of the current densities, in Fig. 14, are similar to those of the temperature except the point (1,1) where the current density rises at first, before falling back to a lower level. The explanation for the dynamic response at the point (1,1) is given below.

At the beginning of the iterations, the mean temperature of the SOLID is relatively low and the consumption rate of the hydrogen in the fuel channels also remains low. Consequently, a large quantity of unused hydrogen reaches the fuel outlet, increasing the local current density near the outlet. As the mean temperature gradually rises with time, the overall hydrogen consumption rate in the stack will increase. Therefore, the hydrogen concentration at the point (1,1) becomes smaller, and the corresponding local current density gradually decreases following the initial increase, as shown in Fig. 14.

Case 2: The fuel flow rate increases by 15% relative to the original rate; the air flow rate is unchanged. The curve of the fuel flow rate is shown in Fig. 15.

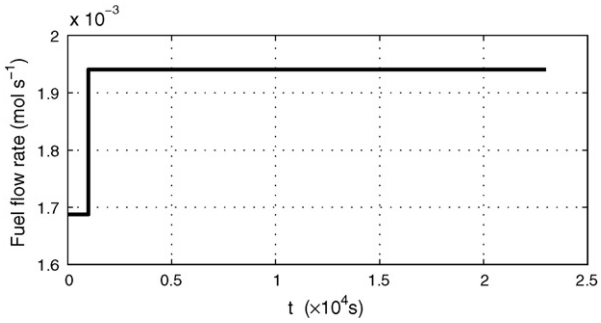

Fig. 15. Curve of the fuel flow rate.

The dynamic responses of the temperature and current density for Case 2 are plotted in Figs. 16 and 17, respectively. The mean temperature and mean current density increase from 1110 K and 1701 A m^{-2}to 1115 K and 1886 A m^{-2} with the increase of the fuel flow rate. However, there are also changes to the temperature and current density curves near the fuel inlet and outlet. Near the fuel inlet (points (0.025, 0.05) and (0.025, 1)), more heat is removed by the accelerated fuel flow. As a result the local temperature gradually decreases, leading to a deceleration of the electrochemical reaction, and the corresponding local current density decrease shown in Fig. 17. On the other hand, the hydrogen concentration as well as the local current density near the fuel outlet (points (1, 0.05) and (1,1)) increases and the corresponding local temperature increases (Fig. 16) due to the accelerated electrochemical reaction. If the fuel flow rate is suffi-

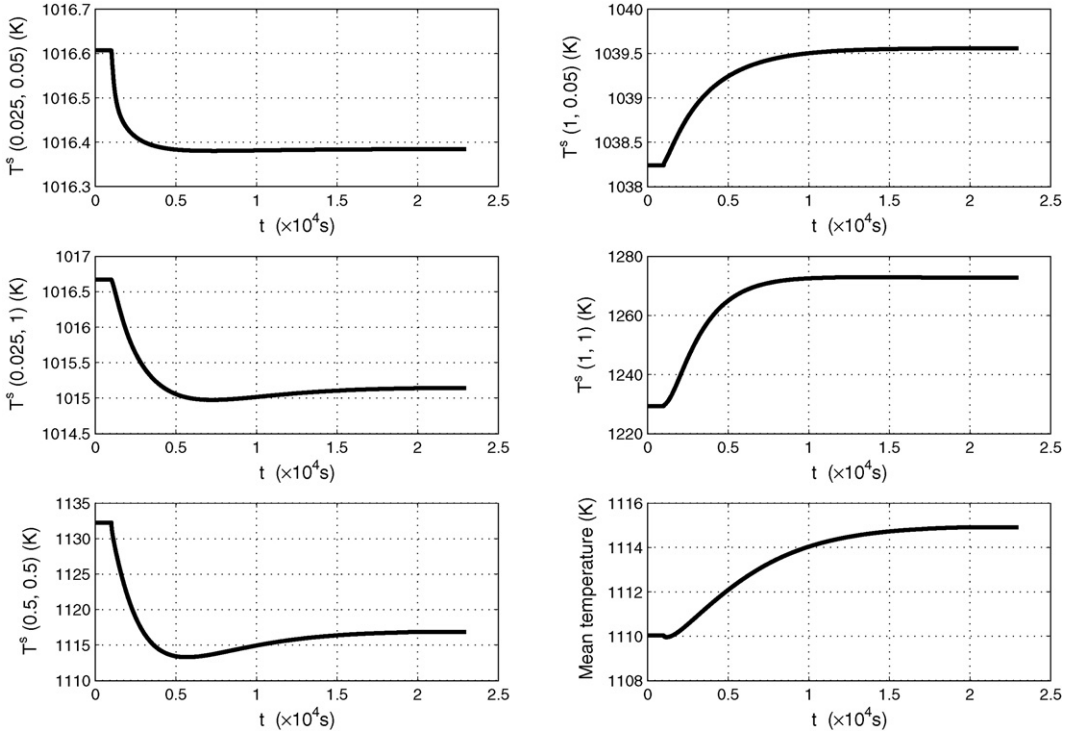

Fig. 16. Dynamic responses of temperature for Case 2.

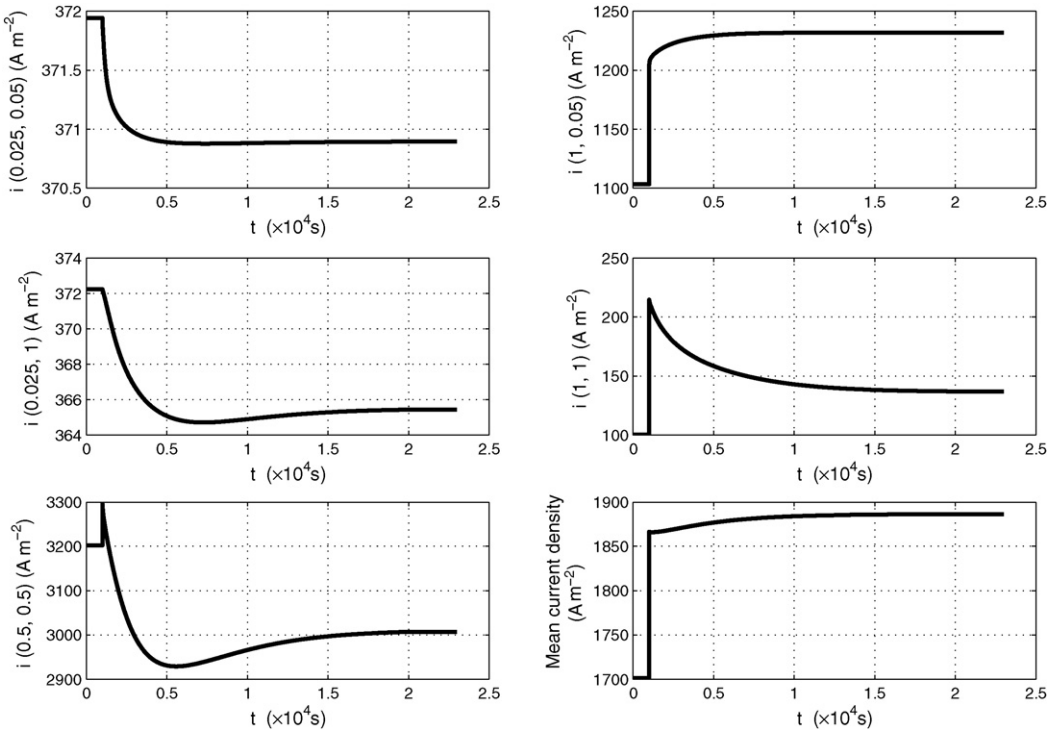

Fig. 17. Dynamic responses of current density for Case 2.

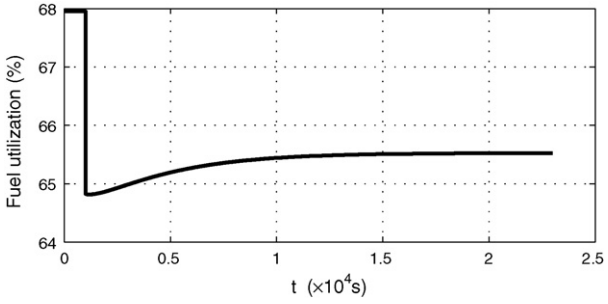

Fig. 18. Dynamic response of fuel utilization for Case 2.

ciently increased, the cooling effect will become the main reason for the reduction of the overall temperature.

Utilization curves for fuel and oxygen are shown in Figs. 18 and 19, respectively. Fuel utilization suddenly decreases following the increase in fuel flow rate, from 67.95% to 64.83%, while the oxygen utilization suddenly increases at this time from 20.86% to 22.87%. Both the fuel and oxygen utilizations then gradually increase because of the intensified mean current density, before stabilizing at 65.52% and 23.12%, respectively. The reduction of the steady-state utilization of the fuel does not imply a decrease in methane consumption. Conversely, more methane is reformed to hydrogen for oxidation in the electrochemical reaction, thus the oxygen utilization for Case 2 increases.

Case 3: The air flow rate decreases by 10% relative to the original rate, while the fuel flow rate is unchanged. Fig. 20 shows the curve of the air flow rate.

The dynamic responses of the temperature and current density for Case 3 are shown in Figs. 21 and 22, respectively. Near the fuel and air inlet, at the point (0.025, 0.05), the local temperature and current density decrease immediately after the step change in the air flow rate. The overall temperature in the stack gradually increases due to the weakened cooling effect of the

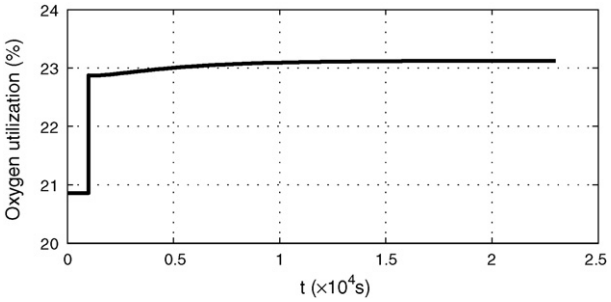

Fig. 19. Dynamic response of oxygen utilization for Case 2.

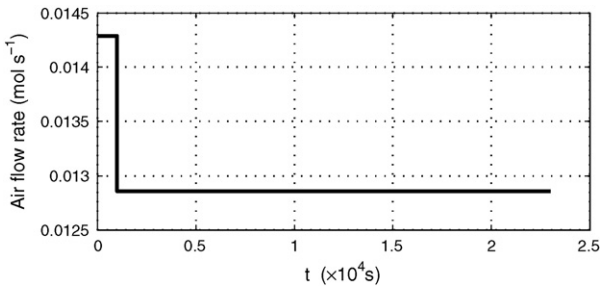

Fig. 20. Curve of the air flow rate.

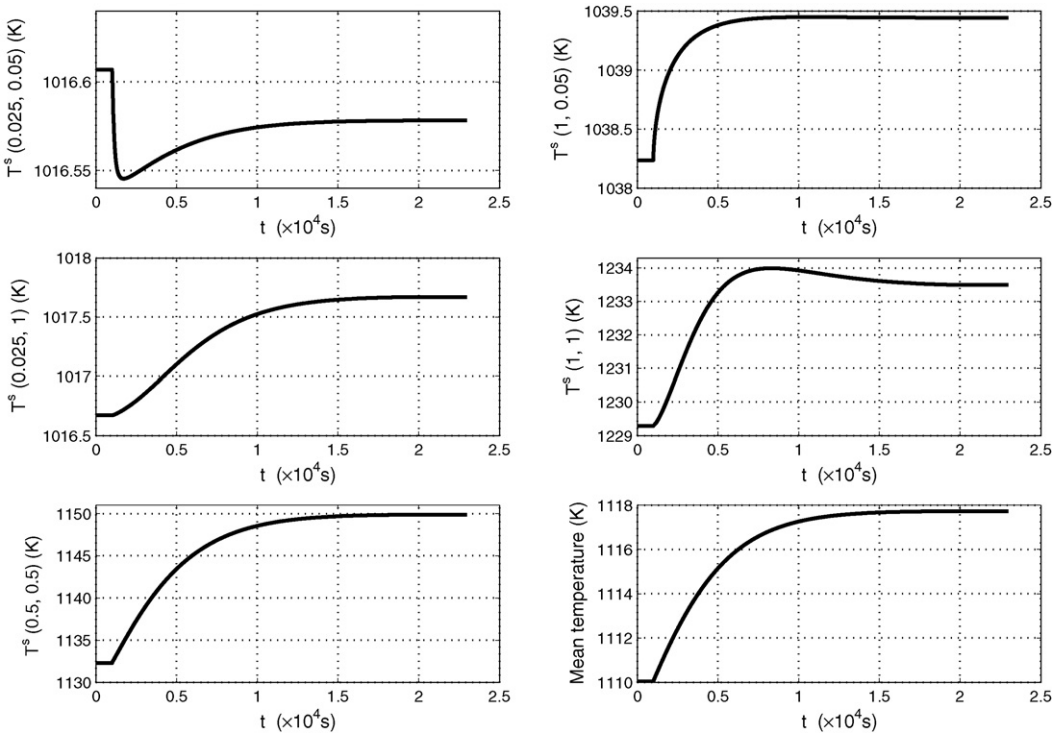

Fig. 21. Dynamic responses of temperature for Case 3.

air flow. The mean temperature and mean current density increase from 1110 K and 1701 A $m^{-2}$to 1117.7 K and 1720.4 A m^{-2}, respectively. Fuel and oxygen utilizations increase, from 67.95% and 20.86% to 68.72% and 23.45% as shown in Figs. 23 and 24, respectively.

Because of the increased consumptions in the stack, the hydrogen and oxygen concentrations reduce at the point (1,1) near the fuel and air outlet, reducing the corresponding local current density, as shown in Fig. 22. However, the corresponding local temperature at the

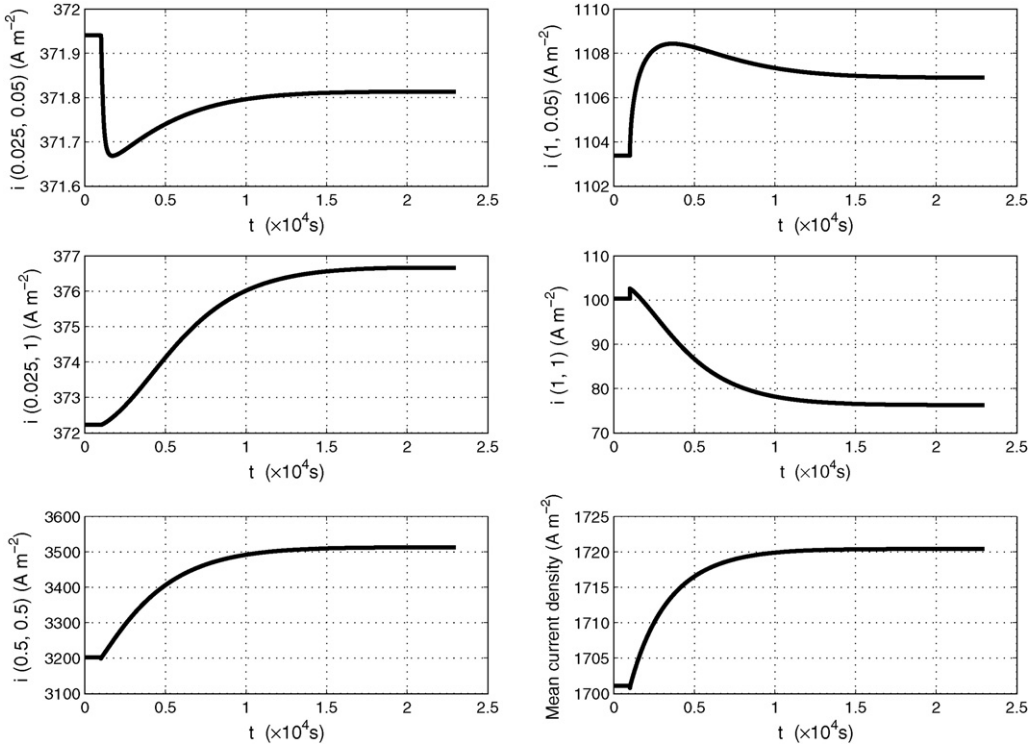

Fig. 22. Dynamic responses of current density for Case 3.

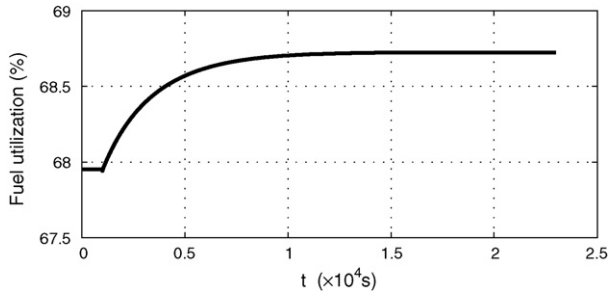

Fig. 23. Dynamic response of fuel utilization for Case 3.

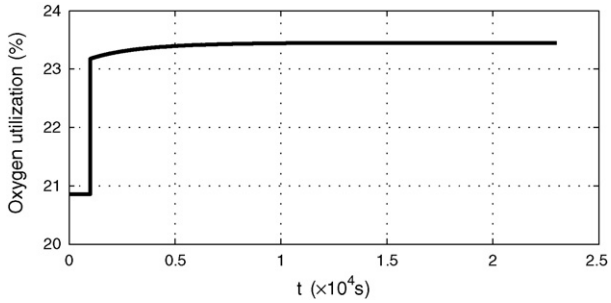

Fig. 24. Dynamic response of oxygen utilization for Case 3.

point (1,1) (Fig. 21) initially increases due to the heat transfer, and then decreases due to the reduced rate of the local electrochemical reaction.

Case 4: The output voltage changes from 0.7 to 0.8 V; the flow rates are unchanged. The output voltage is plotted in Fig. 25.

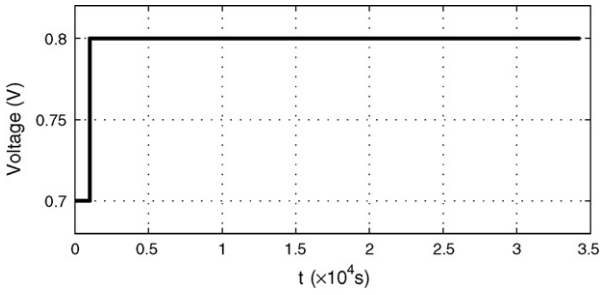

Fig. 25. Curve of the output voltage.

Figs. 26 and 27 show the dynamic responses of the temperature and current density for Case 4, respectively. The temperature and current density generally decrease following the increase of the output voltage. The mean temperature reduces from 1110 to 993 K, and the mean current density from 1701 to 623.5 A m^{-2}. The heat generated is greatly reduced due to the decrease in mean current density. A substantial fraction of hydrogen and oxygen is not consumed in the electrochemical reaction, which increases the concentrations of the hydrogen and oxygen near the outlet following the step change in output voltage. Consequently, the local current density at the point (1,1) increases for about 8000 s, and the resulting heat generated raises the corresponding local temperature for around 3000 s. However, the overall drop of the stack temperature lowers the outlet temperature, decreasing the corresponding local current density. Fuel utilization decreases from 67.95% to 24.91% as shown in Fig. 28,

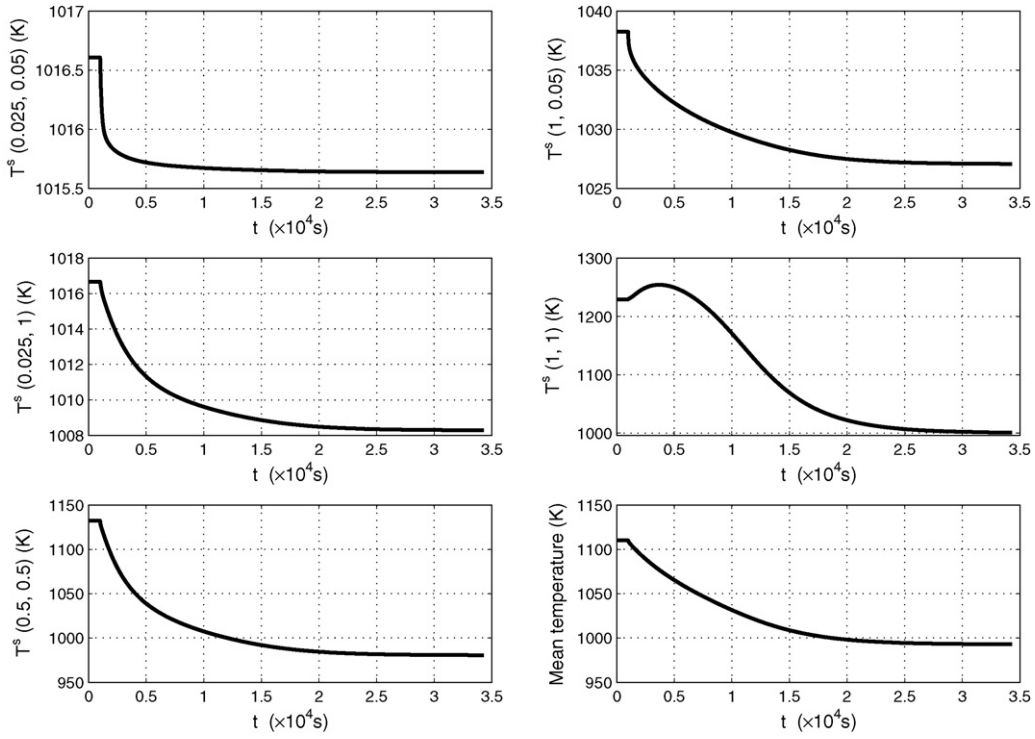

Fig. 26. Dynamic responses of temperature for Case 4.

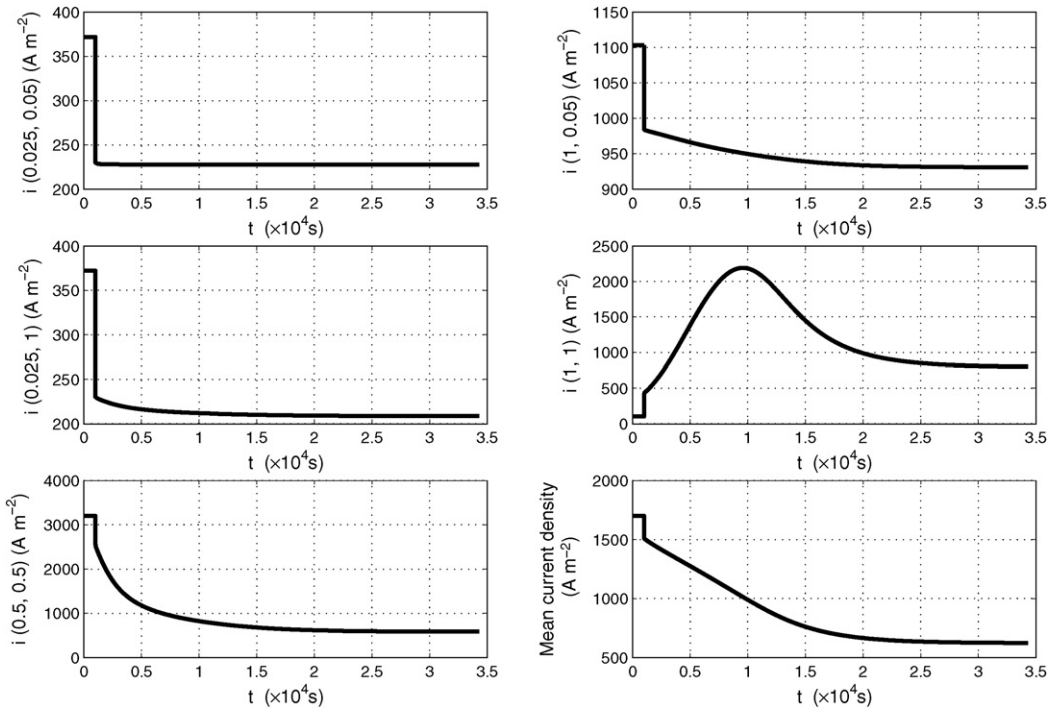

Fig. 27. Dynamic responses of current density for Case 4.

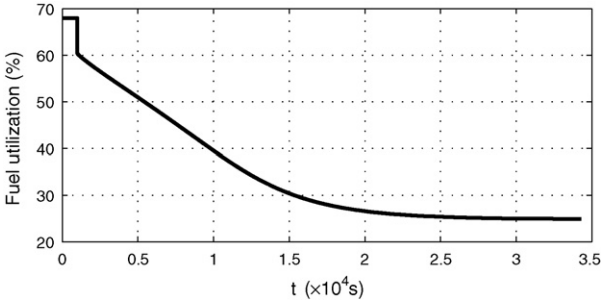

Fig. 28. Dynamic response of fuel utilization for Case 4.

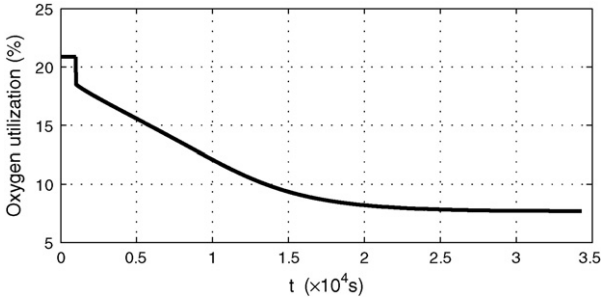

Fig. 29. Dynamic response of oxygen utilization for Case 4.

and the oxygen utilization decreases from 20.86% to 7.69% as shown in Fig. 29.

5. Conclusions

A two-dimensional dynamic DIR-SOFC model has been presented based on the reforming reaction kinetics, the electrochemical model and the transfer principles of mass and heat. Four cases, comprising standard conditions, a fuel flow rate step change, an air flow rate step change and a voltage step change, are used to stimulate the numerical model to obtain the steady states and dynamic responses of the DIR-SOFC. Distributions of temperature, current density and the molar fractions of chemical species; dynamic responses at representative points; and the variations in fuel and oxygen utilizations, are presented to reveal the performances of the cross-flow stack. The results show that the temperature gradients on the SOLID are sufficiently large that they should be considered in design and controlling of the stack. The fuel flow rate, air flow rate and voltage can influence the distributions of the stack parameters. The dynamic responses at different points on the SOLID are not the same. In Case 2, the increase in the fuel flow rate increased the mean current density and mean temperature; the fuel utilization decreased, while the oxygen utilization increased. However, when the fuel flow rate is sufficiently increased, the cooling effect will yield a decreased temperature. In Case 3, the mean temperature as well as the mean current density increased with the decrease in the air flow rate due to a weakened cooling effect. Therefore, the fuel and oxygen utilizations also increased. Results from these simulations show that the fuel and air flow rates should be balanced between the performance improvement and the temperature optimization in practical applications. In Case 4, the increase in the output voltage decreased the mean current density and the generated heat. Hence, the mean temperature and utilizations both decreased.

There are still many problems that have not been resolved completely in this area, such as the optimization and control of the DIR-SOFC. Future work will concentrate on the optimization of modeling and control, to improve the performances of the DIR-SOFC stack.

Acknowledgements

This work is supported by National 863 Scientific Project Development Funds (No. 2006AA05Z148), PR China. The authors also wish to acknowledge Dr. Yang Zhang who has provided helpful discussions.

Appendix A. Matrix form representation of the model equations

The model equations are presented in matrix form as follows:

$$\mathrm{diag}(\vec{\delta})\cdot\mathrm{diag}(\vec{\rho}_{x,y})\cdot\mathrm{diag}(\vec{C}^{\mathrm{st}}_{p,x,y})\cdot\mathrm{diag}(\dot{\vec{T}}_{x,y}) = \mathrm{diag}(\vec{\varphi}_1)+\mathrm{diag}(\vec{\varphi}_2), \tag{A.1}$$

$$\vec{\delta} = (\delta^{\mathrm{up}}, \delta^{\mathrm{an}}, \delta^{\mathrm{s}}, \delta^{\mathrm{ca}}, \delta^{\mathrm{lp}})^T, \tag{A.2}$$

$$\vec{\rho} = (\rho^{\mathrm{up}}, \rho^{\mathrm{an}}, \rho^{\mathrm{s}}, \rho^{\mathrm{ca}}, \rho^{\mathrm{lp}})^T, \tag{A.3}$$

$$\vec{C}^{\mathrm{st}}_p = (C^{\mathrm{up}}_p, C^{\mathrm{an}}_p, C^{\mathrm{s}}_p, C^{\mathrm{ca}}_p, C^{\mathrm{lp}}_p)^T, \tag{A.4}$$

$$\dot{\vec{T}} = (\dot{T}^{\mathrm{up}}, \dot{T}^{\mathrm{an}}, \dot{T}^{\mathrm{s}}, \dot{T}^{\mathrm{ca}}, \dot{T}^{\mathrm{lp}})^T, \tag{A.5}$$

where $\vec{\delta}$ is the thickness vector, $\vec{\rho}$ is the density vector, $\vec{C}_p$ is the specific heat capacity vector, $\vec{T}$ is the temperature vector, diag(·) denotes the diagonal matrix and the subscripts "x, y"denote the co-ordinates (x, y). The matrices introduced on the right hand side of Eq. (A.1) are:

$$\vec{\varphi}_1 = (\varphi^{\mathrm{up}}_1, \varphi^{\mathrm{an}}_1, \varphi^{\mathrm{s}}_1, \varphi^{\mathrm{ca}}_1, \varphi^{\mathrm{lp}}_1)^T, \tag{A.6}$$

$$\vec{\varphi}_2 = (\varphi^{\mathrm{up}}_2, \varphi^{\mathrm{an}}_2, \varphi^{\mathrm{s}}_2, \varphi^{\mathrm{ca}}_2, \varphi^{\mathrm{lp}}_2)^T, \tag{A.7}$$

$$\varphi^{\mathrm{up}}_1 = \delta^{\mathrm{up}}\zeta^{\mathrm{up}}\begin{bmatrix}0\\ \Delta u^{-2}\\ 0\\ 0\\ \Delta w^{-2}\\ 0\end{bmatrix}^T\begin{bmatrix}TM^{\mathrm{up}}_{x,y} & 0\\ 0 & TM^{\mathrm{up}\,T}_{x,y}\end{bmatrix}\begin{bmatrix}1\\ -2\\ 1\\ 1\\ -2\\ 1\end{bmatrix}, \tag{A.8}$$

$$\varphi^{\mathrm{an}}_1 = \Delta u^{-1}\Delta w^{-1}\begin{bmatrix}\vec{F}^{\mathrm{an}}_{x-1,y}\\ \vec{F}^{\mathrm{an}}_{x,y}\end{bmatrix}^T\begin{bmatrix}\vec{C}^{\mathrm{an}}_{p,x-1,y} & 0\\ 0 & \vec{C}^{\mathrm{an}}_{p,x,y}\end{bmatrix}\times\begin{bmatrix}T^{\mathrm{an}}_{x-1,y}\\ -T^{\mathrm{an}}_{x,y}\end{bmatrix}, \tag{A.9}$$

$$\varphi^{\mathrm{s}}_1 = \delta^{\mathrm{s}}\zeta^{\mathrm{s}}\begin{bmatrix}0\\ \Delta u^{-2}\\ 0\\ 0\\ \Delta w^{-2}\\ 0\end{bmatrix}^T\begin{bmatrix}TM^{\mathrm{s}}_{x,y} & 0\\ 0 & TM^{\mathrm{s}\,T}_{x,y}\end{bmatrix}\begin{bmatrix}1\\ -2\\ 1\\ 1\\ -2\\ 1\end{bmatrix}, \tag{A.10}$$

$$\varphi^{\mathrm{ca}}_1 = \Delta u^{-1}\Delta w^{-1}\begin{bmatrix}\vec{F}^{\mathrm{ca}}_{x,y-1}\\ \vec{F}^{\mathrm{ca}}_{x,y}\end{bmatrix}^T\begin{bmatrix}\vec{C}^{\mathrm{ca}}_{p,x,y-1} & 0\\ 0 & \vec{C}^{\mathrm{ca}}_{p,x,y}\end{bmatrix}\times\begin{bmatrix}T^{\mathrm{ca}}_{x,y-1}\\ -T^{\mathrm{ca}}_{x,y}\end{bmatrix}, \tag{A.11}$$

$$\varphi^{\mathrm{lp}}_1 = \delta^{\mathrm{lp}}\zeta^{\mathrm{lp}}\begin{bmatrix}0\\ \Delta u^{-2}\\ 0\\ 0\\ \Delta w^{-2}\\ 0\end{bmatrix}^T\begin{bmatrix}TM^{\mathrm{lp}}_{x,y} & 0\\ 0 & TM^{\mathrm{lp}\,T}_{x,y}\end{bmatrix}\begin{bmatrix}1\\ -2\\ 1\\ 1\\ -2\\ 1\end{bmatrix}, \tag{A.12}$$

$$TM_{x,y} = \begin{bmatrix}0 & T_{x,y-1} & 0\\ T_{x-1,y} & T_{x,y} & T_{x+1,y}\\ 0 & T_{x,y+1} & 0\end{bmatrix}, \tag{A.13}$$

$$\varphi^{\mathrm{up}}_2 = (-q^{\mathrm{up,an}}_{\mathrm{conv}} + q^{\mathrm{s,up}}_{\mathrm{rad}})_{x,y}, \tag{A.14}$$

$$\varphi^{\mathrm{an}}_2 = (q^{\mathrm{an}}_{\mathrm{shift}} + q^{\mathrm{s,an}}_{\mathrm{conv}} + q^{\mathrm{up,an}}_{\mathrm{conv}} - q^{\mathrm{an}}_{\mathrm{react,e}} - q^{\mathrm{an}}_{\mathrm{react,I}} - q^{\mathrm{an}}_{\mathrm{react,II}} + q^{\mathrm{s}}_{\mathrm{react,e}} + q^{\mathrm{s}}_{\mathrm{react,I}} + q^{\mathrm{s}}_{\mathrm{react,II}})_{x,y}, \tag{A.15}$$

$$\varphi^{\mathrm{s}}_2 = (q^{\mathrm{s}} - q^{\mathrm{s,an}}_{\mathrm{conv}} - q^{\mathrm{s,ca}}_{\mathrm{conv}} - q^{\mathrm{s,up}}_{\mathrm{rad}} - q^{\mathrm{s,lp}}_{\mathrm{rad}} - q^{\mathrm{s}}_{\mathrm{react,e}} - q^{\mathrm{s}}_{\mathrm{react,I}} - q^{\mathrm{s}}_{\mathrm{react,II}} + q^{\mathrm{an}}_{\mathrm{react,e}} + q^{\mathrm{an}}_{\mathrm{react,I}} + q^{\mathrm{an}}_{\mathrm{react,II}} + q^{\mathrm{ca}}_{\mathrm{react,e}})_{x,y}, \tag{A.16}$$

$$\varphi^{\mathrm{ca}}_2 = (q^{\mathrm{s,ca}}_{\mathrm{conv}} + q^{\mathrm{lp,ca}}_{\mathrm{conv}} - q^{\mathrm{ca}}_{\mathrm{react,e}})_{x,y}, \tag{A.17}$$

$$\varphi^{\mathrm{lp}}_2 = (-q^{\mathrm{lp,ca}}_{\mathrm{conv}} + q^{\mathrm{s,lp}}_{\mathrm{rad}})_{x,y}. \tag{A.18}$$

In Eqs. (A.15)–(A.17), $q^{\mathrm{an}}_{\mathrm{react},n}$, $q^{\mathrm{ca}}_{\mathrm{react},n}$ and $q^{\mathrm{s}}_{\mathrm{react},n}$ can be written as a general equation to facilitate matrix operations:

$$q^{l}_{\mathrm{react,n}} = D^{l,\mathrm{L}}_n\cdot[\mathrm{diag}(\vec{T})\otimes(\vec{r}\cdot\vec{C}_p{}^T)]\cdot D^{l,\mathrm{R}}_n,\quad l=\mathrm{an,s,ca},\quad n=\mathrm{I,II,e}, \tag{A.19}$$

where $D^{l,\mathrm{L}}_n$ and $D^{l,\mathrm{R}}_n$ are the left and right factor matrixes, respectively, and ⊗ denotes Kronecker product. Each of these quantities has the following components:

$$\vec{C}_p = (C_{p,\mathrm{CH_4}}, C_{p,\mathrm{CO}}, C_{p,\mathrm{CO_2}}, C_{p,\mathrm{H_2O}}, C_{p,\mathrm{H_2}}, C_{p,\mathrm{O_2}}, C_{p,\mathrm{N_2}})^T, \tag{A.20}$$

$$\vec{T} = (T^{\mathrm{up}}, T^{\mathrm{an}}, T^{\mathrm{s}}, T^{\mathrm{ca}}, T^{\mathrm{lp}})^T, \tag{A.21}$$

$$D^{l,\mathrm{L}}_n = (\vec{d}^{\,l,\mathrm{L}}_{n,1}, \vec{d}^{\,l,\mathrm{L}}_{n,2}, \vec{d}^{\,l,\mathrm{L}}_{n,3}, \vec{d}^{\,l,\mathrm{L}}_{n,4}, \vec{d}^{\,l,\mathrm{L}}_{n,5}), \tag{A.22}$$

$$D^{l,\mathrm{R}}_n = (\vec{d}^{\,l,\mathrm{R}}_{n,1}, \vec{d}^{\,l,\mathrm{R}}_{n,2}, \vec{d}^{\,l,\mathrm{R}}_{n,3}, \vec{d}^{\,l,\mathrm{R}}_{n,4}, \vec{d}^{\,l,\mathrm{R}}_{n,5})^T. \tag{A.23}$$

(1) The electrochemical reaction

The components of $D^{\mathrm{s,L}}_{\mathrm{e}}$ and $D^{\mathrm{s,R}}_{\mathrm{e}}$ corresponding to $q^{\mathrm{s}}_{\mathrm{react,e}}$ are

$$\vec{d}^{\,\mathrm{s,L}}_{\mathrm{e},1} = \vec{d}^{\,\mathrm{s,L}}_{\mathrm{e},2} = \vec{d}^{\,\mathrm{s,L}}_{\mathrm{e},4} = \vec{d}^{\,\mathrm{s,L}}_{\mathrm{e},5} = (0,0,0,0,0), \tag{A.24}$$

$$\vec{d}_{e,3}^{s,L} = (0, 0, 0, 1, 0), \quad (A.25)$$

$$\vec{d}_{e,1}^{s,R} = \vec{d}_{e,2}^{s,R} = \vec{d}_{e,4}^{s,R} = \vec{d}_{e,5}^{s,R} = (0, 0, 0, 0, 0, 0, 0), \quad (A.26)$$

$$\vec{d}_{e,3}^{s,R} = (0, 0, 0, 1, 0, 0, 0). \quad (A.27)$$

The components of $D_e^{an,L}$ and $D_e^{an,R}$ corresponding to $q_{react,e}^{an}$ are

$$\vec{d}_{e,1}^{an,L} = \vec{d}_{e,3}^{an,L} = \vec{d}_{e,4}^{an,L} = \vec{d}_{e,5}^{an,L} = (0, 0, 0, 0, 0), \quad (A.28)$$

$$\vec{d}_{e,2}^{an,L} = (0, 0, 0, 1, 0), \quad (A.29)$$

$$\vec{d}_{e,1}^{an,R} = \vec{d}_{e,3}^{an,R} = \vec{d}_{e,4}^{an,R} = \vec{d}_{e,5}^{an,R} = (0, 0, 0, 0, 0, 0, 0), \quad (A.30)$$

$$\vec{d}_{e,2}^{an,R} = (0, 0, 0, 0, 1, 0, 0). \quad (A.31)$$

The components of $D_e^{ca,L}$ and $D_e^{ca,R}$ corresponding to $q_{react,e}^{ca}$ are

$$\vec{d}_{e,1}^{ca,L} = \vec{d}_{e,2}^{ca,L} = \vec{d}_{e,3}^{ca,L} = \vec{d}_{e,5}^{ca,L} = (0, 0, 0, 0, 0), \quad (A.32)$$

$$\vec{d}_{e,4}^{ca,L} = (0, 0, 0, 0, 1), \quad (A.33)$$

$$\vec{d}_{e,1}^{ca,R} = \vec{d}_{e,2}^{ca,R} = \vec{d}_{e,3}^{ca,R} = \vec{d}_{e,5}^{ca,R} = (0, 0, 0, 0, 0, 0, 0), \quad (A.34)$$

$$\vec{d}_{e,4}^{ca,R} = (0, 0, 0, 0, 0, 1, 0). \quad (A.35)$$

(2) Reaction I

The components of $D_I^{s,L}$ and $D_I^{s,R}$ corresponding to $q_{react,I}^{s}$ are

$$\vec{d}_{I,1}^{s,L} = \vec{d}_{I,2}^{s,L} = \vec{d}_{I,4}^{s,L} = \vec{d}_{I,5}^{s,L} = (0, 0, 0, 0, 0), \quad (A.36)$$

$$\vec{d}_{I,3}^{s,L} = (1, 0, 0, 0, 0), \quad (A.37)$$

$$\vec{d}_{I,1}^{s,R} = \vec{d}_{I,2}^{s,R} = \vec{d}_{I,4}^{s,R} = \vec{d}_{I,5}^{s,R} = (0, 0, 0, 0, 0, 0, 0), \quad (A.38)$$

$$\vec{d}_{I,3}^{s,R} = (0, 0, 1, 0, 4, 0, 0). \quad (A.39)$$

The components of $D_I^{an,L}$ and $D_I^{an,R}$ corresponding to $q_{react,I}^{an}$ are

$$\vec{d}_{I,1}^{an,L} = \vec{d}_{I,3}^{an,L} = \vec{d}_{I,4}^{an,L} = \vec{d}_{I,5}^{an,L} = (0, 0, 0, 0, 0), \quad (A.40)$$

$$\vec{d}_{I,2}^{an,L} = (1, 0, 0, 0, 0), \quad (A.41)$$

$$\vec{d}_{I,1}^{an,R} = \vec{d}_{I,3}^{an,R} = \vec{d}_{I,4}^{an,R} = \vec{d}_{I,5}^{an,R} = (0, 0, 0, 0, 0, 0, 0), \quad (A.42)$$

$$\vec{d}_{I,2}^{an,R} = (1, 0, 0, 2, 0, 0, 0). \quad (A.43)$$

(3) Reaction II

The components of $D_{II}^{s,L}$ and $D_{II}^{s,R}$ corresponding to $q_{react,II}^{s}$ are,

$$\vec{d}_{II,1}^{s,L} = \vec{d}_{II,2}^{s,L} = \vec{d}_{II,4}^{s,L} = \vec{d}_{II,5}^{s,L} = (0, 0, 0, 0, 0), \quad (A.44)$$

$$\vec{d}_{II,3}^{s,L} = (0, 1, 0, 0, 0), \quad (A.45)$$

$$\vec{d}_{II,1}^{s,R} = \vec{d}_{II,2}^{s,R} = \vec{d}_{II,4}^{s,R} = \vec{d}_{II,5}^{s,R} = (0, 0, 0, 0, 0, 0, 0), \quad (A.46)$$

$$\vec{d}_{II,3}^{s,R} = (0, 1, 0, 0, 3, 0, 0). \quad (A.47)$$

The components of $D_{II}^{an,L}$ and $D_{II}^{an,R}$ corresponding to $q_{react,II}^{an}$ are

$$\vec{d}_{II,1}^{an,L} = \vec{d}_{II,3}^{an,L} = \vec{d}_{II,4}^{an,L} = \vec{d}_{II,5}^{an,L} = (0, 0, 0, 0, 0), \quad (A.48)$$

$$\vec{d}_{II,2}^{an,L} = (0, 1, 0, 0, 0), \quad (A.49)$$

$$\vec{d}_{II,1}^{an,R} = \vec{d}_{II,3}^{an,R} = \vec{d}_{II,4}^{an,R} = \vec{d}_{II,5}^{an,R} = (0, 0, 0, 0, 0, 0, 0), \quad (A.50)$$

$$\vec{d}_{II,2}^{an,R} = (1, 0, 0, 1, 0, 0, 0). \quad (A.51)$$

References

[1] J. Larminie, A. Dicks, Fuel Cell Systems Explained, Wiley, New York, 2000.

[2] J.H. Hirschenhofer, D.B. Stauffer, R.R. Engleman, M.G. Klett, Fuel Cell HandBook, fourth ed., Parsons Corporation, Reading, PA, 1998, for U.S. Department of Energy, November.

[3] S.H. Clarke, A.L. Dicks, K. Pointon, T.A. Smith, A. Swann, Catal. Today 38 (1997) 411–423.

[4] J. Palsson, A. Selimovic, L. Sjunnesson, J. Power Sources 86 (1) (2000) 442–448.

[5] P. Costamagna, L. Magistri, A.F. Massardo, J. Power Sources 96 (2) (2001) 352–368.

[6] S.H. Chan, H.K. Ho, Y. Tian, J. Power Sources 109 (1) (2002) 111–120.

[7] F. Calise, A. Palombo, L. Vanoli, J. Power Sources 158 (1) (2006) 225–244.

[8] P. Costamagna, K. Honegger, J. Electrochem. Soc. 145 (11) (1998) 3995–4007.

[9] J. Padulles, G.W. Ault, J.R. McDonald, J. Power Sources 86 (1) (2000) 495–500.

[10] W. Jiang, R.X. Fang, J.A. Khan, R.A. Dougal, J. Power Sources 162 (1) (2006) 316–326.

[11] R. Kandepu, L. Imsland, B.A. Foss, C. Stiller, B. Thorud, O. Bolland, Energy 32 (4) (2007) 406–417.

[12] F. Calise, M.D. d'Accadia, A. Palombo, L. Vanoli, Energy 31 (15) (2006) 3278–3299.

[13] E. Achenbach, J. Power Sources 49 (1–3) (1994) 333–348.

[14] P. Aguiar, C.S. Adjiman, N.P. Brandon, J. Power Sources 138 (1–2) (2004) 120–136.

[15] P. Aguiar, C.S. Adjiman, N.P. Brandon, J. Power Sources 147 (1) (2005) 136–147.

[16] J.G. Xu, G.F. Froment, AIChE J. 35 (1) (1989) 88–96.

[17] R. Peters, R. Dahl, U. Kluttgen, C. Palm, D. Stolten, J. Power Sources 106 (1) (2002) 238–244.

[18] P. Vernoux, J. Guindet, M. Kleitz, J. Electrochem. Soc. 145 (10) (1998) 3487–3492.

[19] T. Yamamura, H. Tagawa, T. Saito, J. Mizusaki, K. Kamitani, K. Hirano, S. Ehara, T. Tagaki, Y. Hishinuma, H. Sasaki, T. Sogi, Y. Nakamura, K. Hashimoto, Solid Oxide Fuel Cells (SOFC-IV), in: M. Dokiya, O. Yamamoto, H. Tagawa, S.C. Singhal (Eds.), The Electrochemical Society Proceedings Series PV 95-1, second ed., 1995, p. 741.

[20] M. Mogensen, T. Lindegaard, Solid Oxide Fuel Cells (SOFC-III), in: S.C. Singhal, H. Iwahara (Eds.), The Electrochemical Society Poceedings Series PV 93-4, second ed., 1993, p. 484.

[21] P. Wesseling, Principles of Computational Fluid Dynamics, Springer-Verlag, New York, 2000.